Comparison between Assisted and Dual Phase synchronous reluctance machines for high speed applications

Iman Kleilat, Leila Nguimpi Langue, Guy Friedrich, Stéphane Vivier, Khadija El Kadri Benkara

Comparison between Assisted and Dual Phase synchronous reluctance machines for high speed applications

Iman Kleilat , Leila Nguimpi Langue, Guy Friedrich, Stephane Vivier, Khadija El Kadri Benkara
Sorbonne Universités Université de Technologie de Compiegne, FRE 2012, Roberval
Centre de recherche de Royallieu, CS 60319, 60203 COMPIEGNE CEDEX, FRANCE
iman.kleilat@utc.fr, guy.friedrich@utc.fr, stephane.vivier@utc.fr, khadija.el-kadri-benkara@utc.fr

***Abstract*—This paper proposes a comparison between an Assisted Synchronous Reluctance Machine (SyRMA) and a non-assisted synchronous machine for which a Dual Phase (DP) material is used in the rotor's structure (SyRMDP). Both types of machines, that must operate at high speeds, are designed thanks to the same optimization approach. However, the SyRMA model includes an analytic model which takes into account the mechanical stress on the magnetic bridges due to the centrifugal force in high speed operations. The performance of these two optimally designed machines are compared for applications up to 15000 rpm.**

Keywords— high speed, synchronous reluctance machines, optimization, mechanical stress

I. INTRODUCTION

During the past years, the price of rare earth materials, used in the construction of permanent magnet machines, has increased rapidly [1]. With the need of a moderate cost of efficient motors, especially for hybrid vehicle applications, synchronous reluctance machines appear to be the most qualified to rival permanent magnet machines in terms of cost and performance. The Synchronous reluctance machine was first introduced by Kostko [2] in 1923. And so far these machines have gained a remarkable development encouraged by advances in the design of the rotors. The rotor of a synchronous reluctance machine presents two distinct axes: an axis by which the passage of the magnetic field is easier (axis *d*), and an axis having a stronger reluctance by which the magnetic field circulates with more difficulty (axis *q*). The rotor is positioned with respect to the f.m.m. so that the magnetic field flows through the path with lower reluctance. Therefore the saliency ratio (ratio between the inductances L_d of the *d* axis and L_q of the *q* axis) can quantify the level of magnetic imbalance between these two axes. Accordingly, a higher saliency ratio reflects higher performances.

$$\xi = L_d / L_q \tag{1}$$

Between the different types of rotor architectures of synchronous reluctance machines, the present study examines the case of machines with flux barriers [3] [4]. Flux barriers are non-magnetic cavities in the rotor body that divert the flow of the magnetic field so that it is forced to cross the air gap. They are an essential mean of improving the saliency ratio of a synchronous reluctance machine mainly by the reduction of the quadrature inductance L_q. Fig. 1 represents the ideal case of the flux barriers synchronous reluctance machine.

On the other hand, in order to create the required mechanical strength, the rotor should be manufactured with the different solid parts of the rotor linked together, forcing the flux barriers to be filled at the air gap. This creates very thin iron parts between cavities and the outer surface (especially towards the air gap). These are magnetic bridges. However, from a magnetic point of view, these iron bridges behave like magnetic short circuits: field lines that circulate inside the bridges do not participate in the creation of the torque, because they do not cross the air gap. This can significantly reduce the saliency ratio and therefore the performance of the machine. In order to solve this problem, two realistic solutions can be considered. The addition of ferrite permanent magnets to conventional Synchronous Reluctance machines (SyRM), which yields SyRMA (Assisted) machines allows us to accelerate the saturation of the magnetic bridges (Fig.2). These machines are of strong interest [5-7]. On the other hand, some papers describe a new material, called Dual Phase, for which it is possible to locally modify the magnetic properties [8]. Dual phase materials can be used to replace classical ferromagnetic materials, especially in magnetic bridges. More specifically, when used for the realization of SyRM to give the SyRMDP (Fig.3), it becomes interesting to reduce the permeability of the magnetic bridges with magnetic characteristics close to those of air ($\mu_r = 1$).

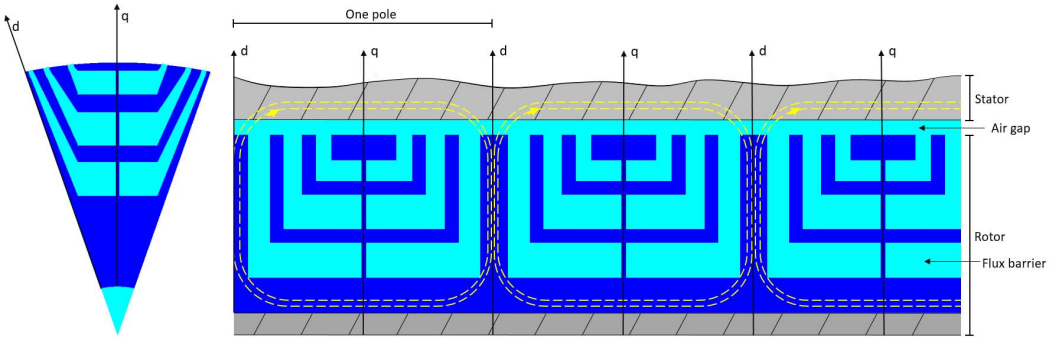

Fig. 1. Ideal synchronous reluctance machine with flux barriers
Flux barriers opens directly onto the air gap

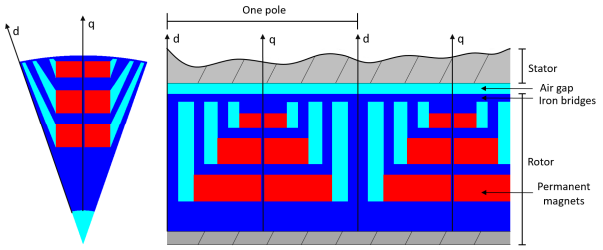

Fig. 2. Assisted synchronous reluctance machine

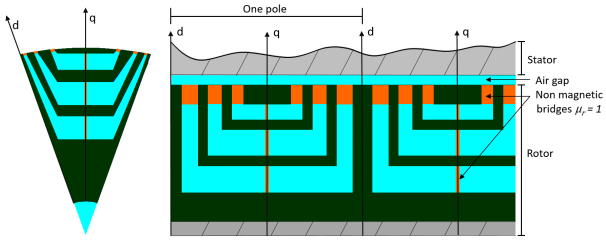

Fig. 3. Dual phase synchronous reluctance machine

Dual phase materials have a high saturation limit of about 1.5 T [8] (which remains lower than that of the regular silicon steel used for conventional SyRM) (Fig.4).

In high speed application, the problem of the mechanical robustness of the rotor becomes a fundamental issue which cannot be neglected. In fact, the mass of the active part of the rotor imposes, due to centrifugal forces, very high mechanical stresses on magnetic bridges. Under these conditions, the mechanical elastic limits of materials can be reached. This can imply reducing the maximum rotational speed, depending on the rotor geometry. Moreover, this limitation of the mechanical speed impacts the maximum power density of the machine. Hence, from a mechanical point of view, designing thicker magnetic bridges can handle the mechanical strength weakness of the machine when working at high speed. However, the optimization of the electromagnetic performance, tends to reduce their thicknesses. In the case of the SyRMDP, thicknesses of magnetic bridges are theoretically unconstrained and do not impact the performance of the machine since they are non-magnetic and thus, there is no limitation for the mechanical speed. For SyRMA, permanent magnets are used to saturate the magnetic bridges and thus enhance the performance of the machine. But also, the insertion of permanent magnets in flux barriers compromise the structural behavior of the rotor specially for high speeds. For all these reasons, it becomes crucial to make optimizations dedicated for high speed application, that integrate mechanical constraints.

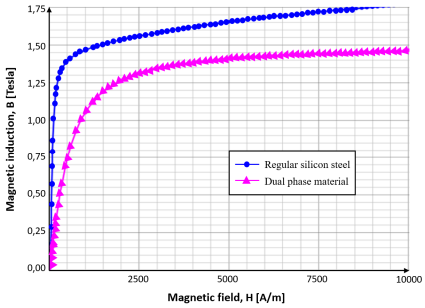

Fig. 4. B(H) curve of regular silicon steel and DP material

In an attempt to find the most robust synchronous reluctance machine with the best performance in terms of power, efficiency and power factor, this paper presents an optimization of the two types of machines (SyRMA and SyRMDP) for high speed applications. For the SyRMA, a performance optimization of the rotor with the use of a coupled electromagnetic and structural study is presented. The optimization considers a finite element electromagnetic model with a simple analytic mechanical model presented in the following section, to evaluate mechanical stresses over the rotor. The objective is to integrate (high speed) mechanical aspects as constraints into the optimization process. For the SyRMDP, only an electromagnetic performance optimization is needed. It is done using a finite element electromagnetic model. The mechanical stress is not taken into account, insofar as theoretically, thanks to this new material, the mechanical performance become independent of the width of the bridges. Then a comparison between the two machines optimized for high speed applications (up to 15000 rpm) is carried out.

II. MECHANICAL MODEL

When operating at high speed, mechanical strength limits of materials can be reach. Recent papers are trying to handle mechanical problems of synchronous reluctance machines. However, with the use of decoupled electromagnetic and structural study, poor performance has been detected [9] [10]. In terms of analysis method, mechanical finite element analyses are mainly used with the purpose of observing the maximum stresses and checking the mechanical strength of the rotor [11-13]. Analytic model proposals are also available in the literature to evaluate these mechanical constraints and to integrate them into an optimization process [14-16]. In this article, a simple analytic model based on the "Beam Theory" to calculate mechanical stresses, is developed. Iron bridges in the rotor of SyRM machines, can be considered as simple rectangular section beams where the thicknesses of the iron bridges "e_a" and "e_c" and the stack length "l", define the dimensions of the beams (Fig. 5). This analytic model is then directly integrated into the optimization of the geometry in order to obtain at the same time high-performance and robust machines.

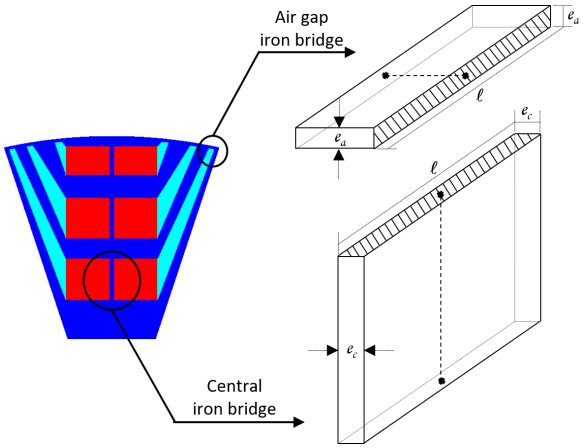

Fig. 5. Beam representation of the bridges

A. Beam theory

The beam theory, owing to its simplicity, stands as an important tool in structural and mechanical engineering. By definition, any solid engendered by a plane section whose center of gravity describes a curve is considered as a beam. Two of the dimensions of a beam are relatively small to the third, and the section may be constant or continuously variable.

In order to obtain faster solutions, this approach considers some simplifying assumptions related to the conditions of reversibility and linearity [17].

- Material: The material of the beam is homogenous, continuous and isotropic.
- Small disturbances assumption: deflections are assumed to be very small.
- Saint-Venant's assumption: at a point away from the supports and efforts points of application, the effect of the load is almost independent of the way the latter is applied.
- Superposition principle: the resulting final deflection of the beam subject to a combination of loads, is simply the sum of the deflections caused by each of the individual loads. This principle depends on the elastic behavior of the material.
- Bernoulli's hypothesis: after deformation, the straight sections of a beam remain plane and perpendicular to the average line. This goes to the global assumption of small perturbations.

a) Cohesion torsor of a beam

The cohesion torsor (2) is used to represent the internal efforts arising in the beam that directly depend on the action of a set of external forces acting on the beam. In Fig. 6 the associated cohesion torsor represents the action of one part over the other. To a certain limit, these interactions maintain the cohesion of the material. Depending on the type of the load (tension/compression, shear, flexion ...), some elements of the cohesion torsor become null.

$$\vec{T}_{cohesion} = \left\{ \begin{matrix} \vec{R}_G \\ \vec{M}_G \end{matrix} \right\} \tag{2}$$

Accordingly, the term "stress" is used to describe the surface density of the forces exerted on the beam and it is calculated by the following equation:

$$\vec{\sigma} = \lim_{dS \to 0} \frac{d\vec{T}_{cohesion}}{dS} \tag{3}$$

The vector stress can be decomposed into its normal component $\vec{\sigma}_n$ and its projection on the section $\vec{\sigma}_t$. The relation between the two components is given by:

$$\|\vec{\sigma}\|^2 = \|\vec{\sigma}_n\|^2 + \|\vec{\sigma}_t\|^2 \tag{4}$$

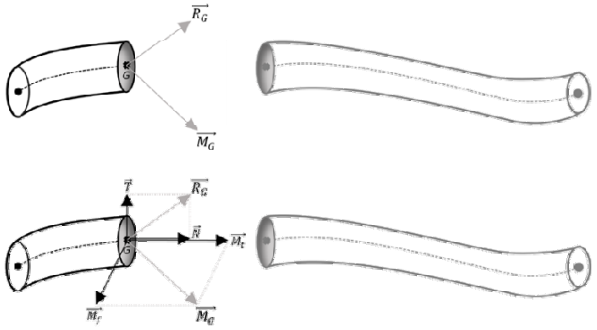

Fig. 6. Cohesion torsor of a beam

b) Some types of loads

Tension /compression:

When a beam is in traction, only the normal effort $\vec{N}$ of the cohesion torsor is not zero, and with the previous assumptions, it is considered that this force is constant along the beam. The cohesion torsor is then written as:

$$\overrightarrow{R_G}\left|\begin{matrix}\vec{N} \neq 0 \\ \vec{T} = 0\end{matrix}\right. \quad and \quad \overrightarrow{M_G}\left|\begin{matrix}\overrightarrow{M_t} = 0 \\ \overrightarrow{M_f} = 0\end{matrix}\right.$$

Once the efforts are identified and quantified, the stresses within the beam can be described using the following equation.

$$\sigma_n = \frac{N}{S} \tag{5}$$

Flexion:

When the beam is in flexion, the cohesion torsor becomes:

$$\overrightarrow{R_G}\left|\begin{matrix}\vec{N} = 0 \\ \vec{T} \neq 0\end{matrix}\right. \quad and \quad \overrightarrow{M_G}\left|\begin{matrix}\overrightarrow{M_t} = 0 \\ \overrightarrow{M_f} \neq 0\end{matrix}\right.$$

The tangential stress is expressed as described by the following equation.

$$\sigma_t = \frac{T}{S} \tag{6}$$

The normal flexion stress is expressed as:

$$\sigma_{M_f} = \frac{M_f \times y}{I} \tag{7}$$

Where,

- I: the quadratic moment of inertia calculated with respect to the axis passing through the center of gravity of the section.
- y: variable representing the algebraic dimension between the neutral fiber and a point in the beam section.

In our case, $I = \frac{l \times e_{a,c}^3}{12}$ and $y = \frac{e_{a,c}}{2}$.

Then the total flexion stress becomes:

$$\sigma_f = \sqrt{\sigma_t^2 + \sigma_{M_f}^2} \tag{8}$$

c) Stress concentration

The stress concentration is a phenomenon that occurs when the cross-section of a part varies in a brutal way due to holes and grooves. This results in a local increase of stresses in this area. To illustrate this problem in a simple way, one can take the example of a plate stressed in traction. The density of isolines can be used as a level indicator of traction stresses. Without the presence of the hole, the stress lines are equally spaced. With the presence of the hole, it is found that these lines are disturbed around the latter and that the density increases (Fig. 7). It means that the maximum real stress is larger than the mean value given by the beam theory equations.

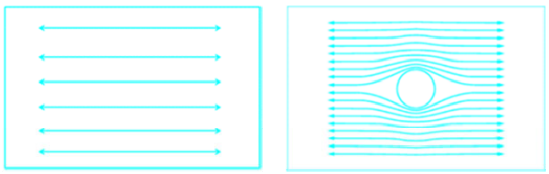

Fig. 7. Qualitative schematic illustration showing the origin of stress concentration

d) Theoretical coefficient of stresses concentration

K_t is defined as the ratio of the maximum real stress in the discontinuity zone to the maximum nominal stress:

$$K_t = \frac{\sigma_{real}}{\sigma_{nom}} \quad (9)$$

The index "*t*" is used to indicate that these coefficients are theoretical and that their calculation is based on the beam theory assumptions.

σ_{nom} is the maximum nominal stress that can be calculated using material resistance formulas, considering the part as a beam or a plate without taking into account the geometric discontinuities.

σ_{real} is the maximum real stress that can be calculated using numerical methods such as the finite element method or analytical methods for simple geometries.

The theoretical coefficient of stress concentration K_t depends on the part geometry and the type of stress. In this case, it is assumed that the mechanical components' material is homogeneous and continuous. Below are the assumed hypotheses for the use of K_t:

- stresses are static
- real stresses are calculated as if the material had a purely elastic behavior

B. Analytic model

a) From rotor pole to beam structure

Based on a previous study of the stress magnitudes in the rotor [18], it has been shown that the highest stresses are located inside iron bridges: the central iron bridge and the air gap iron bridges (Fig. 5). From a modeling point of view, iron bridges are considered as simple rectangular section beams. Such a configuration allows the use of the beam theory in order to perform an analytic modeling of the mechanical stresses (Fig. 8).

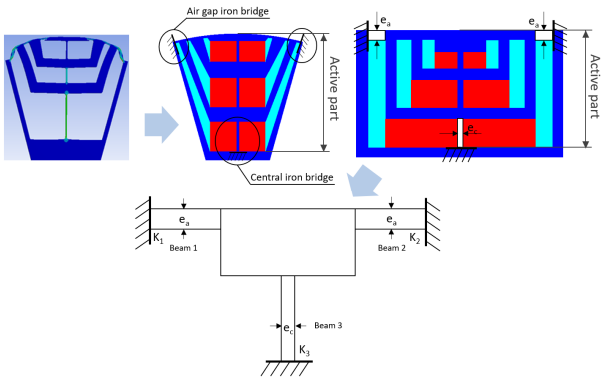

Fig. 8. From rotor pole to beam structure

Each pole of the rotor is considered as embedded with the adjacent poles at the air gap iron bridges (K_1 and K_2), and with the rotor body at the central iron bridge (K_3).

b) From centrifugal force to mechanical efforts

The centrifugal force (10) is the main source of stress within iron bridges. It is considered applied at point G, the center of mass of the active part which is defined as the outer ring of the rotor containing the iron parts between the cavities (as well as the magnets for the SyRMA).

$$F_{centrifuga\ l} = m \times R_G \times \Omega^2 \quad (10)$$

Where,

- m is the mass of the active part of one pole [kg]
- R_G is the distance between the center of the rotor and the center of gravity G of the active part of the pole [m]
- Ω is the rotational speed of the rotor [rad.s^{-1}]

Referring to the analysis of the rotor deformations due to centrifugal forces, and in order to know their distribution in one rotor pole, it is assumed that beams 1 and 2 undergo flexion stress and beam 3 a traction stress. This assumption allows to obtain the effort configuration shown in Fig. 9. In this case the cohesion torsor can be described as

$$\overrightarrow{R_{K12}}\left|\begin{matrix}\vec{N}=0\\ \vec{T}\neq 0\end{matrix}\right. \quad \overrightarrow{M_{K12}}\left|\begin{matrix}\overrightarrow{M_t}=0\\ \overrightarrow{M_f}\neq 0\end{matrix}\right.$$

and

$$\overrightarrow{R_{K3}}\left|\begin{matrix}\vec{N}\neq 0\\ \vec{T}=0\end{matrix}\right. \quad \overrightarrow{M_{K3}}\left|\begin{matrix}\overrightarrow{M_t}=0\\ \overrightarrow{M_f}=0\end{matrix}\right.$$

After identifying the mechanical efforts on the active part of the rotor, the nominal stresses within this structure can be deduced from (5) and (8).

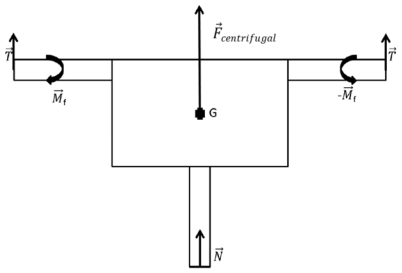

Fig. 9. Efforts on the active part of one rotor pole

C. Model calibration

In order to analytically determine the maximum real stresses in iron bridges, one must:

1. Find the relationship between the normal effort N, the tangential effort T and the flexion moment M_f to the centrifugal force. This allows us to calculate σ_{nom}.
2. Determine the theoretical concentration coefficients of stresses K_t, and find σ_{real}.

1) Relationship between N, M_f, T and $F_{centrifugal}$

Based on the centrifugal force presented in (10) and on off-line finite element analyses done in previous works, it is possible collect data for different cases of calculation: different speeds (variation of Ω) and different thicknesses of iron bridges (variation of m and R_G) (Table I).

Table I

Thickness (mm)	0.3	0.9	1.5
m (kg)	0.145	0.146	0.147
R_G (mm)	48	48	48

(a) Mass and rotational radius of the active part

Thickness (mm) /Speed (rpm)	0.3	0.9	1.5
10 000	7 632.5	7 685.1	7 737.8
14 000	14 959.7	15 062.8	15 166.0
18 000	24 729.3	24 899.8	25 070.4

(b) Centrifugal force [N] according to speed and thickness of iron bridges

It has been shown that the functions connecting the centrifugal force to the normal effort, the tangential effort and the flexion moment, are independent of the thicknesses of iron bridges. Then, the curves in Fig. 10 show that there is a linear relationship between the centrifugal force and these three efforts. Then the following equations can be deduced:

$$N = A \times F_{centrifugal} \quad (11)$$

$$T = B \times F_{centrifugal} \quad (12)$$

$$M_f = C \times F_{centrifugal} \quad (13)$$

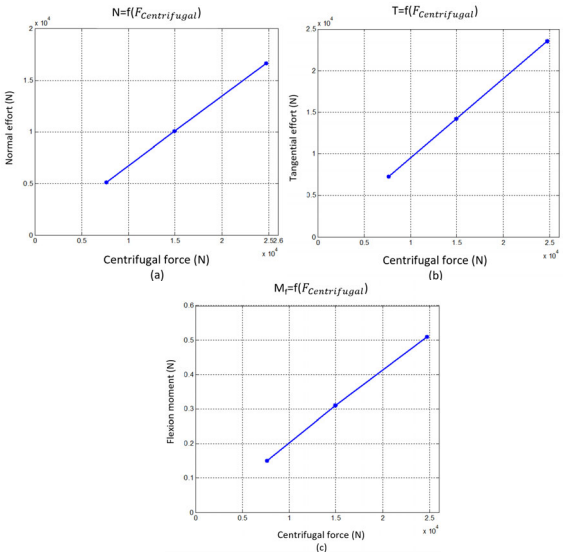

Fig. 10. Curves of efforts with respect to centrifugal force (a) Normal effort, (b) Tangential effort, (c) Flexion moment

2) K_t coefficients

The concentration coefficients of the different stresses (traction and flexion) are determined thanks to the finite element calculation of the nominal maximum stress and real maximum stress. These coefficients depend only on the thickness of the iron bridges. Fig. 11a shows a linear relation between the concentration coefficient of traction stress on beam 3 "K_{tn}" (normal effort) and the central iron bridge thickness e_c. Fig. 11b presents the relation between the coefficient of concentration of flexion stress on beam 1 and 2 "K_{tf}" (tangential effort and flexion moment) and the air gap iron bridges thickness e_a. The input / output law between these two quantities is not perfectly linear, but can be linearized without major consequences on the estimation of the actual maximum stresses. It follows that:

$$K_{tn} = D \times e_c + H \quad (14)$$

$$K_{tf} = J \times e_a + M \quad (15)$$

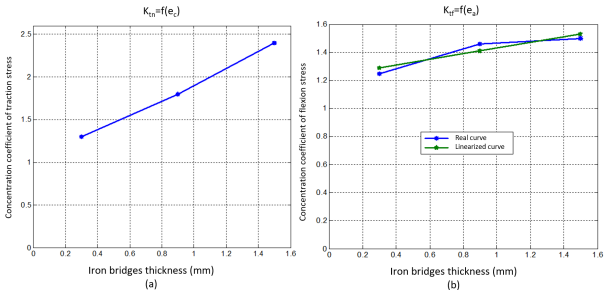

Fig. 11. Curve of the concentration coefficient (a) of traction stress K_{tn}, (b) of flexion stress K_{tf}

To summarize, the formulas for determining the real maximum traction and flexion stresses are:

$$\sigma_{b3} = \sigma_{nreal} = K_{tn} \times \sigma_n = \frac{A \times \Omega^2}{l} \times m \times R_G \times (D + \frac{H}{e_c}) \quad (16)$$

$$\sigma_{b12} = \sigma_{freal} = K_{tf} \times \sigma_f = \frac{\sqrt{B^2 + (6 \times \frac{C}{ea})^2} \times \Omega^2}{l} \times m \times R_G \times (J + \frac{M}{e_a}) \quad (17)$$

Constants for (16) and (17), deduced from the previous curves, are gathered in Table II.

Table II Constant values for the calculation of mechanical stresses

A	B	C	D	H	J	M
0.67	1	$2*10^{-5}$ m	10^4 m^{-1}	1	$0.2*10^3$ m^{-1}	1.23

At this stage, there is a calibrated analytic model that allows the determination of high speed mechanical stresses. This model being very fast to calculate, is adapted to be used within an optimization design approach.

III. Performance Optimization

One of the most important indicator of an electric machine performance is the developed electromagnetic torque. It can be expressed as follows:

$$T_{em} = f(\xi, (I_{RMS}, \beta), \psi_f) \quad (18)$$

Then, the optimization process of the flux barrier synchronous reluctance machine is based on two successive stages:

- Parameterization and optimization of the rotor geometry for a single operating point and with fixed current control settings. This step aims to get the best value for the saliency ratio ξ.
- Optimization of the current vector with magnitude I_{RMS} and electrical angle β, for the optimized geometry of the machines.

This process is carried out for both types of machines (SyRMA and SyRMDP). In both cases, each rotor pole has three levels of flux barriers. The numerous geometric and electric variables involved, the complexity of the rotor geometry as well as the strongly non-linear magnetic behavior of materials used in this structure, make the application of finite element analysis compulsory for the computation of the electromagnetic model of the machines.

A. Geometry optimization

The choice is made to focus on the optimization of the rotor geometry and therefore to keep the stator unchanged. 5 (variable) parameters are identified for each flux barrier, giving a total of 15 variables. These parameters are the end barrier opening angle *Ebo*, the end barrier width *Eba*, the bottom barrier width *Bbw* (which also represents the width of the permanent magnet in the case of the assisted rotor), the bottom barrier height *Bbh* and the bottom barrier position *Bbp*. In addition, the central and air gap iron bridges thicknesses e_c and e_a are added. The total number of parameters is therefore 17 for the whole rotor (Fig. 12). Table III gathers all the constant stator values.

By optimizing the geometry, the goal is to find the most adequate set of geometric parameters leading to the best output performance of the machine: that is to say the highest output power and the lowest torque ripples. For this, from the electromagnetic point of view, the most difficult operating point where to perform this optimization is the one at 2 000 rpm in generator mode. For this point, where no flux-weakening is needed, the current vector (I_{RMS}, β) can be fixed. I_{RMS} is determined according to the current density limit in stator coils during nominal operation; implicitly, this allows to take account of thermal considerations. Concerning the current angle β, its value is determined thanks to a magnetostatic finite element analysis (Fig.13).

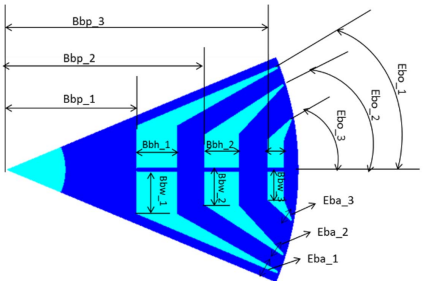

Fig. 12. Geometric variables used in optimization

Table III Main geometric characteristics of the machine

Parameters	Value	Unit
Stator external radius	75.5	mm
Stator slots number	72	
Poles pairs	6	
Rotor internal radius	54.95	mm
Stack length	70	mm

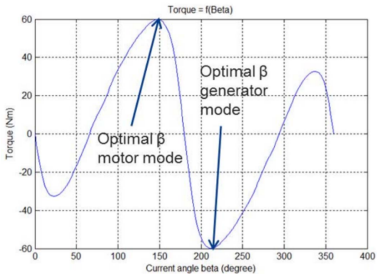

Fig. 13. Torque as function of the current angle β

In addition, voltages applied to the stator coils also need to be controlled since they can induce limitations. Since the machine is powered through an inverter, itself connected to a battery system, it is mandatory to take into account the specific characteristics of these external elements to deduce the actually available voltage amplitude.

In the case of the SyRMA, the optimal design must necessarily take into account the mechanical stresses, calculated analytically in the previous section, which must remain below limit values (stresses must be below the elastic domain limit σ_e). For this reason, the calculation of the centrifugal force is directly influenced by geometric variables. Since geometric parameters define the mass of the active part (m) and its equivalent radius (R_G), they necessarily intervene in the evaluation of the various mechanical stresses (16) and (17).

The optimization of the rotor geometry is achieved by the Differential Evolution (DE) algorithm, a stochastic optimization technique.

B. Optimal current control

Once the optimal architecture of the rotor is computed, the second stage is applied; it consists in seeking optimal values for the current control (current amplitude I_{RMS} and electrical angle β) on the entire reachable power-speed range. An optimal control makes it possible to supply the machine in such a way that its performances meet as much as possible the desired functionality of the system. The choice is made to minimize losses in the machine, while satisfying the constraints imposed by the structure environment (battery and inverter).

The current control optimization is achieved by the Sequential Quadratic Programming (SQP) algorithm; this method is a deterministic optimization technique.

Fig. 14 presents an example of optimal current control for the case of SyRMA. This allows the building of a performance plot defined in the power/torque-speed plane.

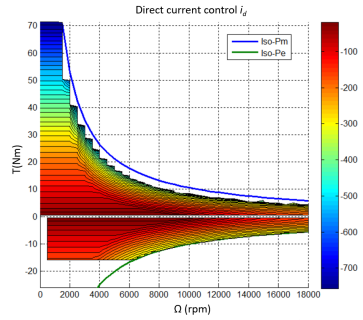

(a) Direct current control in the work space

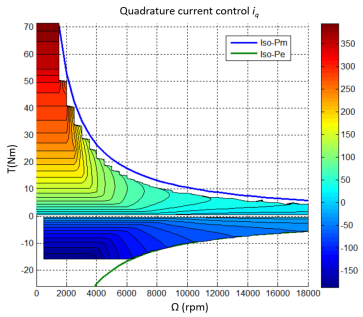

(b) Quadrature current control in the work space

Fig. 14. Optimal current control

To summarize, the optimization of the geometry with fixed control makes it possible to obtain optimal geometries, while the optimal control allows to pilot these machines in the most adequate way in order to exploit their full potential. Thus the problem of optimizing the performance of both SyR machines can be resumed by Table IV.

Table IV Optimization process

Machine type	SyRMA	SyRMDP
Models	Finite element electromagnetic model	
	Analytic mechanical model	
Objective functions	-Maximizing the output power: f_{oP}= max(P_{output}) at 2 000 rpm generator mode. -Minimizing torque ripples: $f_{o\Delta T}$= min(ΔT) at 2 000 rpm generator mode.	
Constraints	Voltage constraint: $V_{RMS} - V_{lim} < 0$	
	Mechanical constraints: $\sigma_{nreal} - \sigma_e < 0$ $\sigma_{freal} - \sigma_e < 0$	
Geometry Tool	Differential evolution algorithm	
Current control Tool	Total losses minimization with SQP algorithm	

C. Results

- The calculated performance are compared to 2 templates: in motor mode for $P_{output} > 0$ (mechanical output power) and in generator mode for $P_{output} < 0$ (electrical output power). The point P_1 is the operating point for which we proceed the optimization: 2 000 rpm in generator mode. Both machines will be compared based on 5 criteria:
- output power at 2 000 rpm in generator mode (at P_1),
- torque ripples "ΔT" (at P_1),
- efficiency "η" (at P_1),
- power factor "f" (at P_1)
- output power at 15 000 rpm in generator mode (at P_2).

Torque ripples are calculated as described by (19), efficiency by (20) and power factor by (21).

$$\Delta T = \left| \frac{T_{\max} - T_{\min}}{T_{\max} + T_{\min}} \right| \tag{19}$$

$$\eta = \left(\frac{P_m}{P_e} \right)^{sign\,(T_{em})} \tag{20}$$

$$f = \frac{P_{output}}{3 \times V_{RMS} \times I_{RMS}} \tag{21}$$

Fig. 15 presents the output power (in motor and generator modes) for the SyRMA and SyRMDP machines and Table V presents a comparison of performance of both optimized machines with respect to the 5 criteria and the resultant saliency ratio calculated after optimization. We can notice that even if the saliency ratio of the SyRMA is smaller than that of the SyRMDP, it presents higher performance. Comparing the output power at point P_2 it becomes clear that SyRMA can perform much better at high speed application (up to 15 000 rpm). The machine using Dual Phase material is less performant. This can be explained by the fact that the induction of saturation of this material is lower (Fig.4).

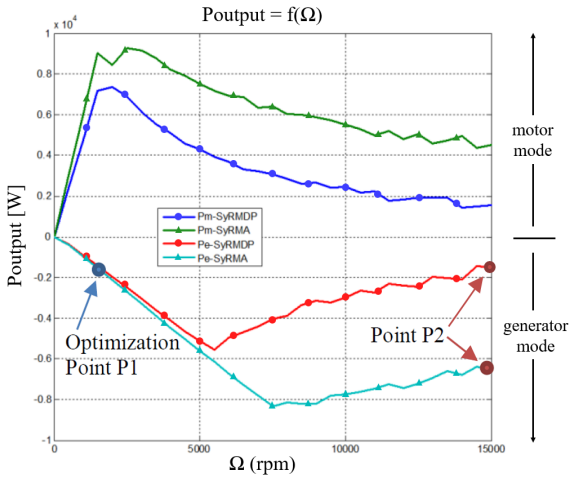

Fig. 15. Output power comparison between SyRMDP and SyRMA

Table V Comparative table of final machines

	SyRMA	SyRMDP
ξ	2.7	2.9
P_{output} (P_1) [kW]	2.1	1.9
ΔT (%)	4.8	5.0
η	0.91	0.90
f	0.62	0.53
P_{output} (P_2) [kW]	6.5	1.6

IV. CONCLUSION

In this paper, an analytic model has been proposed to take into account the rotor mechanical stresses due to high speed application. A reference to the "beam theory" has been made, to take into account the stress concentration due to the specific shape of the magnetic bridges in the SyRM. This model has been integrated in the optimal design of an assisted SyRM dedicated to high speed applications. The dual phase SyRM allows thick magnetic bridges because this type of material theoretically allows local modification of magnetic properties. Performance of dual phase material are issued from literature. The comparison shows that:

- The use of the analytic model allows to determine an "optimal value" for the thickness of the magnetic bridge, yielding the ability to maintain performance and preserve the rotor integrity in high speed applications.
- The consideration of stress concentration is fundamental. This study proposes an analytic method which shows that this phenomenon increases the local stress by a factor 2.5 for the traction mode and a factor 1.6 for the flexion mode.
- Even if dual phase materials seem "ideal" for the considered applications, their magnetic performance need improvement in order to challenge SyRMA in medium speed applications.
- Even if magnetic performance obtained by using dual phase materials remain lower than those obtained with classic materials, it may become interesting to use such DP for high speeds automotive applications (40 000 rpm) since this technology allows wider magnetic bridges and therefore very robust rotors with regard to centrifugal forces.

ACKNOWLEDGMENT

This work is co-funded by the European Union and "Hauts de France" Region. Europe is involved in "Hauts de France" through the European Funds for Regional Development. Thanks to the Lebanese University for also supporting this work.

REFERENCES

[1] Widmer, James D., Richard Martin, and Mohammed Kimiabeigi. "Electric vehicle traction motors without rare earth magnets." Sustainable Materials and Technologies 3 (2015): 7-13.

[2] Kostko, J. K. "Polyphase reaction synchronous motors." Journal of the American Institute of Electrical Engineers 42, no. 11 (1923): 1162-1168.

[3] Kolehmainen, Jere. "Synchronous reluctance motor with form blocked rotor." IEEE Transactions on Energy Conversion 25, no. 2 (2010): 450-456.

[4] Dziechciarz, Arkadiusz, and Claudia Martis. "New shape of rotor flux barriers in synchronous reluctance machines based on Zhukovski curves." In Advanced Topics in Electrical Engineering (ATEE), 2015 9th International Symposium on, pp. 221-224. IEEE, 2015.

[5] Schmidt, Erich, Wolfgang Brandl, and Christian Grabner. "Design improvement of synchronous reluctance machines with internal rotor flux barriers for high-speed drives." In Power Electronics Specialists Conference, 2002. pesc 02. 2002 IEEE 33rd Annual, vol. 4, pp. 1949-1954. IEEE, 2002.

[6] Ferrari, Marco, Nicola Bianchi, Alberto Doria, and Emanuele Fornasiero. "Design of synchronous reluctance motor for hybrid electric vehicles." IEEE Transactions on Industry Applications 51, no. 4 (2015): 3030-3040.

[7] Barcaro, Massimo, Nicola Bianchi, and Freddy Magnussen. "Permanent-magnet optimization in permanent-magnet-assisted synchronous reluctance motor for a wide constant-power speed range." IEEE Transactions on Industrial Electronics 59, no. 6 (2012): 2495-2502.

[8] Reddy, Patel Bhageerath, Ayman M. El-Refaie, Steven Galioto, and James P. Alexander. "Design of synchronous reluctance motor utilizing dual-phase material for traction applications." IEEE Transactions on Industry Applications 53, no. 3 (2017): 1948-1957.

[9] Babetto, Cristian, Giacomo Bacco, and Nicola Bianchi. "Synchronous Reluctance Machine Optimization for High Speed Applications." IEEE Transactions on Energy Conversion (2018).

[10] Di Nardo, Mauro, Giovanni Lo Calzo, Michael Galea, and Chris Gerada. "Design optimization of a high-speed synchronous reluctance machine." IEEE Transactions on Industry Applications 54, no. 1 (2018): 233-243.

[11] Di Nardo, Maura, G. Lo Calzo, Michael Galea, and Chris Gerada. "Structural design optimization of a high speed synchronous reluctance machine." In Electrical Machines (ICEM), 2016 XXII International Conference on, pp. 2073-2079. IEEE, 2016.

[12] Kimiabeigi, M., J. D. Widmer, R. Long, Y. Gao, J. Goss, R. Martin, T. Lisle, JM Soler Vizan, A. Michaelides, and B. Mecrow. "High-performance low-cost electric motor for electric vehicles using ferrite magnets." IEEE Transactions on Industrial Electronics 63, no. 1 (2016): 113-122.

[13] Taghavi, Seyed Morteza, and Pragasen Pillay. "A mechanically robust rotor with transverse laminations for a wide-speed-range synchronous reluctance traction motor." IEEE Transactions on Industry Applications 51, no. 6 (2015): 4404-4414.

[14] Burnand, Guillaume, Douglas Martins Araujo, and Yves Perriard. "Very-high-speed permanent magnet motors: Mechanical rotor stresses analytical model." In Electric Machines and Drives Conference (IEMDC), 2017 IEEE International, pp. 1-7. IEEE, 2017.

[15] Chai, Feng, Yi Li, Peixin Liang, and Yulong Pei. "Calculation of the maximum mechanical stress on the rotor of interior permanent-magnet synchronous motors." IEEE Transactions on Industrial Electronics 63, no. 6 (2016): 3420-3432.

[16] Jannot, Xavier, Jean-Claude Vannier, Claude Marchand, Mohamed Gabsi, Jacques Saint-Michel, and Daniel Sadarnac. "Multiphysic modeling of a high-speed interior permanent-magnet synchronous machine for a multiobjective optimal design." IEEE Transactions on Energy Conversion 26, no. 2 (2011): 457-467.

[17] Hibbeler R. C. " Mechanics of materials 10e. " Pearson 2016.

[18] Langue, Leila Nguimpi, Guy Friedrich, Stephane Vivier, and Khadija El Kadri Benkara. "Consideration of mechanical constraints for an optimal design of ferrite assisted flux-barriers synchronous reluctance machines." In Electric Machines and Drives Conference (IEMDC), 2017 IEEE International, pp. 1-6. IEEE, 2017.